

Unraveling the unusually high electrical conductivity of the delafossite metal PdCoO₂

Xiaoping Yao,^{1,2,3} Ye Chen Xun,^{2,3} Ziye Zhu,^{2,3} Shu Zhao,^{2,3} and Wenbin Li^{2,3,*}

¹School of Materials Science and Engineering, Zhejiang University, Hangzhou 310027, China

²Key Laboratory of 3D Micro/Nano Fabrication and Characterization of Zhejiang Province, School of Engineering, Westlake University, Hangzhou 310030, China

³Institute of Advanced Technology, Westlake Institute for Advanced Study, Hangzhou 310024, China

(Dated: August 9, 2023)

The prototypical delafossite metal PdCoO₂ has been the subject of intense interest for hosting exotic transport properties. Using first-principles transport calculations and theoretical modeling, we reveal that the high electrical conductivity of PdCoO₂ at room temperature originates from the contributions of both high Fermi velocities, enabled by Pd $4d_{z^2} - 5s$ hybridization, and exceptionally weak electron-phonon coupling, which leads to a coupling strength ($\lambda = 0.057$) that is nearly an order of magnitude smaller than those of common metals. The abnormally weak electron-phonon coupling in PdCoO₂ results from a low electronic density of states at the Fermi level, as well as the large and strongly faceted Fermi surface with suppressed Umklapp electron-phonon matrix elements. We anticipate that our work will inform the design of unconventional metals with superior transport properties.

The prototypical delafossite metal PdCoO₂ has attracted considerable interest since its experimental realization for harboring unusual electron transport properties^{1–5}. Despite being an oxide material, PdCoO₂ exhibits an exceptionally low in-plane resistivity of $2.6 \mu\Omega\text{cm}^6$ at room temperature, even comparable to those of the most conducting elemental metals such as copper and silver. Its extremely long electron mean free path, up to 60 nm at room temperature and 20 μm at low temperature^{4,6,7}, also sets a record. Recently, there has been a renaissance of research in PdCoO₂ and a number of new exotic transport phenomena have been uncovered, including the observation of hydrodynamic electron flow and directional ballistic transport^{8–13}.

Understanding the origin of PdCoO₂'s extraordinary transport properties, however, has been a long-standing challenge. Based on the analysis of angle-resolved photoemission spectroscopy data, Noh et al. ascribed PdCoO₂'s high conductivity to its high Fermi velocities, a large two-dimensional (2D) Fermi surface and long carrier lifetimes¹⁴. Combining de Haas–van Alphen and resistivity measurements, Hicks et al. revealed the anomalously low contributions from electron–phonon, electron–electron, and electron–impurity scattering to the in-plane transport of PdCoO₂⁶. A recent study indicates that the unusual high level of crystallinity in PdCoO₂ is responsible for its weak electron-impurity scattering¹⁵. However, a complete understanding of the electron-phonon scattering, which is typically the dominant source of resistivity near room temperature, is still lacking⁴. By carrying out fully *ab initio* transport calculations and theoretical analyses, our work addresses the origin of the weak electron-phonon coupling and high carrier velocities in PdCoO₂, enabling us to provide a comprehensive understanding of the exceptionally high electrical conductivity of PdCoO₂.

PdCoO₂ crystallizes in rhombohedral delafossite-type

structure, with $R\bar{3}m$ space group symmetry. It comprises alternative layers of Pd and edge-shared CoO₆ octahedra flattened with respect to the c -axis, each of which forms an individual triangular lattice, as shown in Fig. 1a. These two alternating layers are connected by the O-Pd-O dumbbells, where Pd is linearly coordinated to two oxygen atoms (see Fig. S1a) and formally in a monovalent state^{14,16,17}.

First, we summarize the first-principles electronic structure of PdCoO₂ in Fig. 1b. Only a single steep band crosses the Fermi level. The strongest contribution near the Fermi level was found to come from Pd. Further orbital decomposition reveals that the states near the Fermi level mainly derive from the $\{d_{z^2}, d_{x^2-y^2}, d_{xy}\}$ orbitals of Pd, and to a lesser extent, the s and p orbitals of Pd (see Fig. S2 and Fig. S3). The associated Fermi surface (see Fig. 1e) is highly two-dimensional and nearly hexagonal⁶.

We obtain the intrinsic, phonon-limited electrical conductivity and resistivity of PdCoO₂ and, for comparison, metal Pd, by solving the linearized Boltzmann transport equation (BTE) with fully *ab initio* electron-phonon coupling^{18,19} (see Supplementary Method). The results are shown in Fig. 1(c,d). The calculated room-temperature in-plane resistivity of PdCoO₂, $2.9 \mu\Omega\text{cm}$, demonstrates a close agreement with the experimental value of $2.6 \mu\Omega\text{cm}^6$. Besides, PdCoO₂ exhibits a strong anisotropy of conductivity, with the in-plane conductivity several hundred times higher than that in the perpendicular direction. This prevailing in-plane character is consistent with its quasi-2D structure. Compared with the pure metal Pd, PdCoO₂ has significantly (more than a factor of three) lower resistivities in all temperature regimes.

To unveil the origin of the exceptionally low in-plane resistivity found in PdCoO₂, we have investigated the key parameters that influence the conductivity of a metal, including Fermi velocity, charge carrier density, and carrier

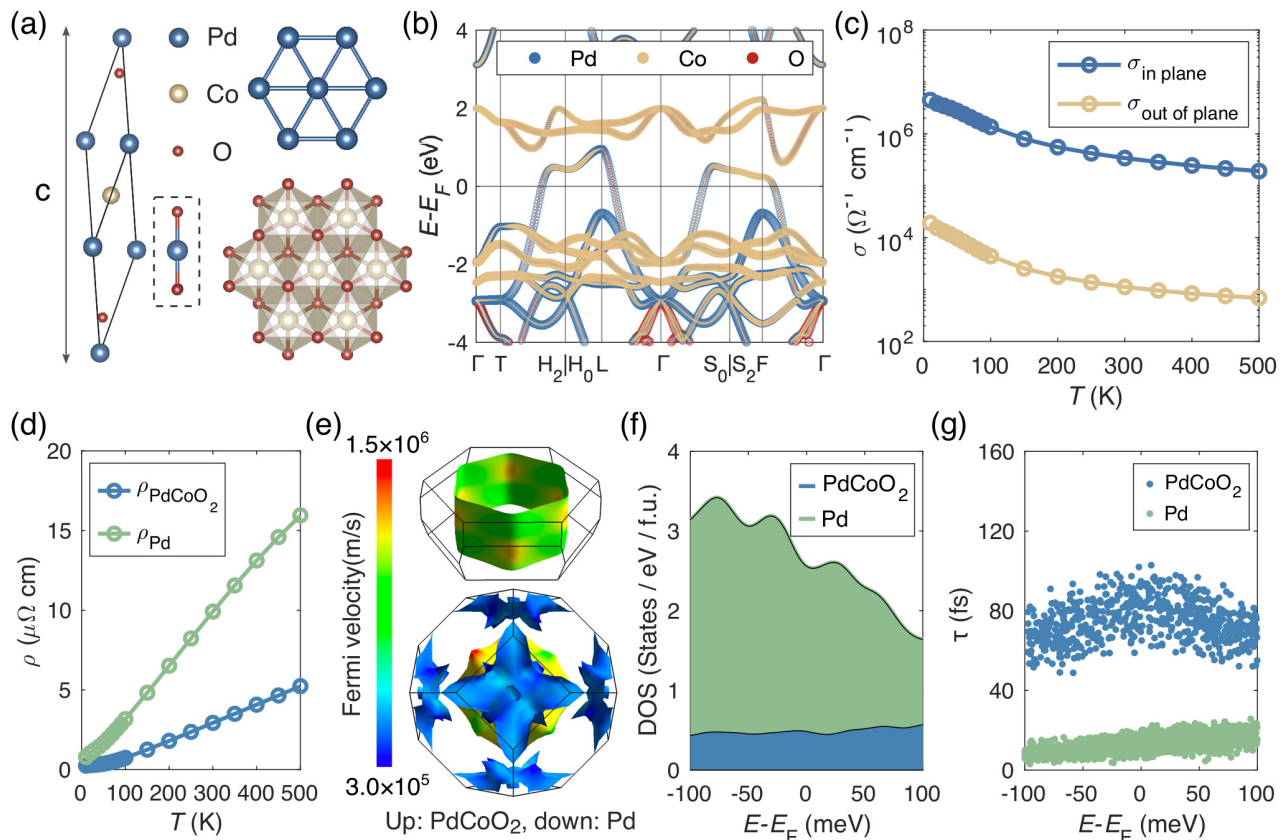


FIG. 1. Atomistic models and electronic transport properties of PdCoO₂. (a) Primitive cell of PdCoO₂, triangular lattice of Pd, and edge-sharing CoO₆ octahedra. The O-Pd-O dumbbell in the dashed box demonstrates the twofold, linearly coordinated environment of Pd. (b) Electronic band structure of PdCoO₂ calculated from density functional theory. The corresponding reciprocal space path is illustrated in Fig. S1b. The atomic orbital characters of the bands are indicated using open circles of different colors. (c) Comparison of the intrinsic electrical conductivity along the in-plane and out-of-plane directions in PdCoO₂, calculated by *ab initio* Boltzmann transport equation. (d) Comparison between the in-plane resistivities of PdCoO₂ and Pd. (e) Fermi velocities of PdCoO₂ (upper panel) and Pd (bottom panel) projected on the corresponding Fermi surfaces. (f) Comparison of the carrier density of states (DOS) per formula unit near the Fermi level of PdCoO₂ and Pd. The zero of the horizontal axis represents the Fermi level. (g) Comparison of the carrier lifetimes of PdCoO₂ and Pd at 300K.

lifetime, and further made a comparison with Pd. The Fermi velocities (v_F) of PdCoO₂ and Pd are projected onto their respective Fermi surface in Fig. 1e, from which it is seen that Pd can have both high and low v_F (see also the band structure of Pd in Fig. S4), whereas PdCoO₂ has relatively uniform and high v_F . It can be deduced that, on average, PdCoO₂ has higher v_F compared with Pd, which contributes to its higher conductivity. Thus, a key issue in understanding PdCoO₂'s high conductivity is the origin of its high Fermi velocities. We will return to this in light of our tight-binding (TB) model. In Fig. 1f, we compare the carrier density of states (DOS) per unit cell near the Fermi level in PdCoO₂ and Pd. It is seen that the DOS of PdCoO₂ is, on average, nearly five times smaller than that of Pd within the 100 meV range around their corresponding Fermi level. Adding the fact that the unit-cell volume of PdCoO₂ is nearly 2.7 times larger than that of Pd, it can be deduced that the charge car-

rier density in PdCoO₂ is significantly lower than that in Pd. In Fig. 1g, we further compare the carrier lifetimes of PdCoO₂ and Pd at 300 K, for energies within the 100 meV range around their corresponding Fermi level. The result demonstrates that PdCoO₂'s carrier lifetimes (about 80 fs) are almost one order of magnitude larger than that of Pd. As a result of the high Fermi velocities and long carrier lifetimes, the in-plane mean free path of PdCoO₂ has large values around 60 nm at room temperature (Fig. S5). On the basis of the above results, it can be concluded that the reason why PdCoO₂ has remarkably high conductivity is that it possesses both highly mobile and extremely long-lived electrons.

We now return to the subject of high Fermi velocities in PdCoO₂, whose origin has been in debate, especially on the role played by the Pd 5s states^{3,6,17,20–24}. Here we illustrate how the high Fermi velocities arise in a TB model. Specifically, we developed a minimal four-band

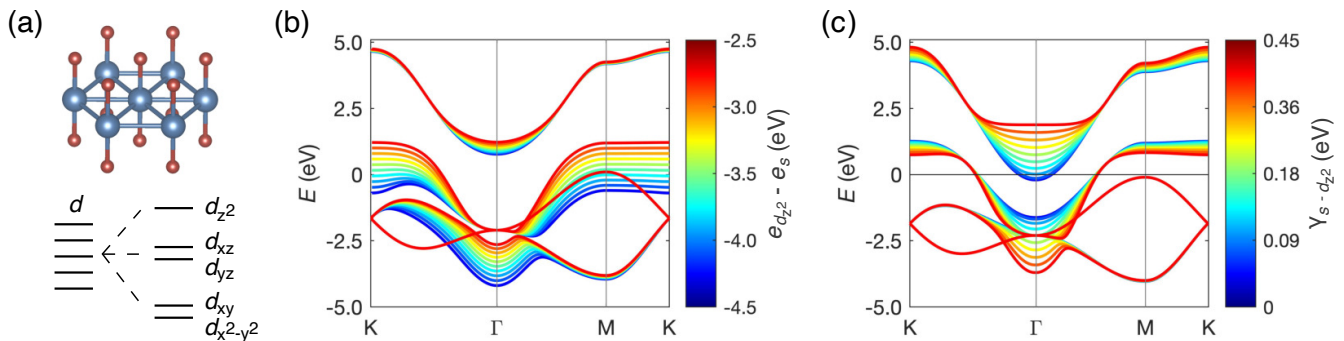


FIG. 2. Origin of the high Fermi velocities in PdCoO₂. (a) The coordinate environment around Pd in PdCoO₂ and the resulting unusual uniaxial crystal field. Each Pd atom (blue ball) is linearly coordinated with two O atoms (red balls), leading to d -orbital splitting, with the d_{z^2} orbital occupying the highest level. (b,c) Evolution of the tight-binding (TB) bandstructure of a corresponding Pd sheet with TB parameters: (b) The on-site energy difference between the $5s$ and $4d_{z^2}$ orbitals $e_{d_{z^2}} - e_s$, and (c) the hopping integral between the $5s$ and $4d_{z^2}$ orbitals $\gamma_{s-d_{z^2}}$.

(s d_{z^2} $d_{x^2-y^2}$ d_{xy}) TB model involving only the nearest-neighbor Pd-Pd hoppings on a simple bare Pd triangular-lattice sheet, with Pd in a monovalent state. The detail of the TB model and can be found in Supplementary Note 1, and the DFT-calculated and TB-fitted band structures are shown in Fig. S6 and Fig. S7, respectively. We then examine the bandstructure evolution by varying the TB parameters, as shown in Fig. 2. With the on-site energy level of the $4d_{z^2}$ orbital increased, the band composed mainly by $4d_{z^2}$ shifts to higher in energy and becomes the only conduction band. The slope of this conduction band (and hence the Fermi velocities) can be effectively increased by increasing the hopping integral between the $5s$ and $4d_{z^2}$ orbitals.

On the basis of the TB model, the high Fermi velocities of PdCoO₂ can be ascribed to the unusual crystal field splitting provided by the unique twofold, linearly coordinated Pd in PdCoO₂, which splits the $4d$ orbitals of Pd into three degenerate subsets, $\{d_{z^2}\}$, $\{d_{xz}, d_{yz}\}$, and $\{d_{xy}, d_{x^2-y^2}\}$, with the $\{d_{z^2}\}$ subset occupying the highest energy, as illustrated in Fig. 2a. The crystal field environment and the reduced energy gap between the $5s$ and $4d_{z^2}$ orbitals also lead to enhanced $5s - 4d_{z^2}$ hybridization³. Together with the monovalent state of Pd, these conditions result in a single, highly dispersive band that crosses the Fermi level. This model is further corroborated by an artificially constructed crystal model of PdF that has a similar structure as PdCoO₂ (see Fig. S8a), in which F atoms replace the CoO₂ layers and serve as electron acceptor, thus allowing Pd to remain in a monovalent state. By controlling the crystal field of Pd through the stretching or compression of the Pd-F distance, we are able to significantly tune the Fermi velocities of the system (see Fig. S8).

The other factor contributing to PdCoO₂'s high conductivity, as mentioned above, is its exceptionally long carrier lifetimes τ , which motivates us to query the reason behind. For metals, when the temperature is

above the Debye temperature, the carrier lifetime can be estimated by $\tau = \hbar(2\pi k_B T \lambda)^{-1}$, where λ is the electron-phonon coupling strength^{25,26}. λ is computed from the Eliashberg spectral function $\alpha^2 F(\omega)$ as $\lambda = 2 \int_0^\infty d\omega \omega^{-1} \alpha^2 F(\omega)$, where $\alpha^2 F(\omega)$ is given by

$$\alpha^2 F(\omega) = \frac{1}{N_F} \sum_{m\nu\nu'} \int \frac{d\mathbf{k}d\mathbf{k}'}{\Omega_{\text{BZ}}^2} |g_{m\nu\nu'}(\mathbf{k}, \mathbf{k}')|^2 \delta(\varepsilon_{n\mathbf{k}} - \varepsilon_F) \times \delta(\varepsilon_{m\mathbf{k}'} - \varepsilon_F) \delta(\hbar\omega - \hbar\omega_{\mathbf{k}'-\mathbf{k}, \nu}). \quad (1)$$

Here, N_F represents the DOS per spin per unit cell at the Fermi level ε_F . The integrations are over the Brillouin zone of volume Ω_{BZ} . $g_{m\nu\nu'}(\mathbf{k}, \mathbf{k}') = \langle \psi_{m\mathbf{k}'} | \Delta_{\mathbf{q}\nu} V_{\text{scf}} | \psi_{n\mathbf{k}} \rangle$ is the electron-phonon matrix element for a Bloch wave with a band index n and momentum \mathbf{k} scattered to another state $m\mathbf{k}'$, due to the variation of the self-consistent potential V_{scf} induced by a phonon with momentum \mathbf{q} and branch index ν . Conservation of crystal momentum requires that $\mathbf{k}' - \mathbf{k} = \mathbf{q} + \mathbf{G}$, with $\mathbf{G} = 0$ and $\mathbf{G} \neq 0$ corresponding to normal and Umklapp scattering, respectively.

In Fig. 3a, we compare the calculated λ and $\alpha^2 F(\omega)$ of PdCoO₂ and Pd. Surprisingly, the coupling strength of PdCoO₂ ($\lambda = 0.057$) is nearly an order of magnitude smaller than that of Pd ($\lambda = 0.36$). It is exceptionally small even compared to other highly conducting metals such as Cu ($\lambda = 0.14$)^{26,27}. This is also reflected in the $\alpha^2 F(\omega)$ of PdCoO₂, whose value is rather small in the low-frequency range, before a peak emerges at a relatively high acoustic-phonon frequency of ~ 20 meV (see also Fig. S9). The peaks in the $\alpha^2 F(\omega)$ of PdCoO₂ at frequencies above 80 meV come from high-frequency optical phonons that correspond to the Pd-O bond stretching/compression modes^{28,29}, but their contribution to λ is relatively minor ($\sim 12\%$, see also Fig. S10). Using the computed λ value, the carrier lifetime of PdCoO₂ at 300 K is estimated to be ~ 71 fs, in close agreement with

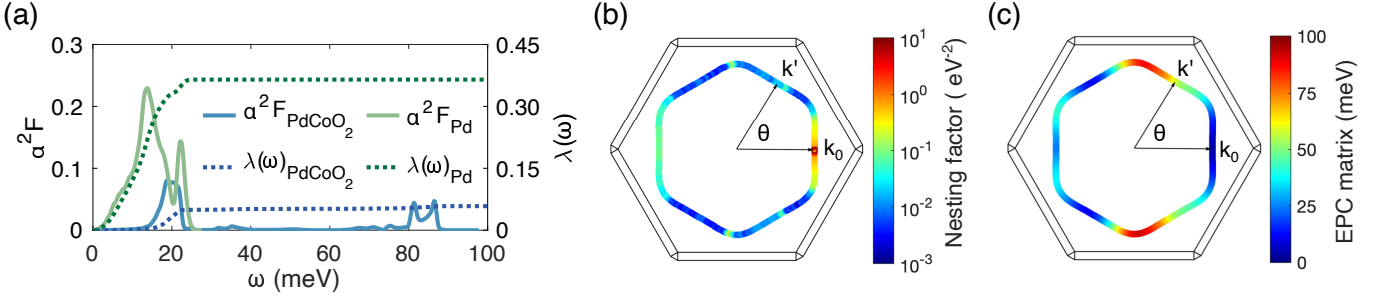


FIG. 3. Electron-phonon coupling in PdCoO₂ and Pd. (a) Comparison of the Eliashberg spectral function $\alpha^2 F(\omega)$ and the associated electron-phonon coupling strength λ between PdCoO₂ and Pd, with the blue and green lines representing PdCoO₂ and Pd, respectively. (b) The nesting factor ($\xi_{\mathbf{k}'-\mathbf{k}_0}$) along a cross section ($k_z = 0$) of the Fermi surface in PdCoO₂, with the initial electronic state fixed at \mathbf{k}_0 and the final located at \mathbf{k}' along the Fermi surface. The angle θ represents the direction of \mathbf{k}' with respect to \mathbf{k}_0 . (c) Sum of the absolute values of the acoustic electron-phonon matrix elements between \mathbf{k}_0 and \mathbf{k}' along the Fermi surface section in PdCoO₂.

the *ab initio* values that average around 80 fs. We have also computed the transport Eliashberg spectral function $\alpha_{\text{tr}}^2 F(\omega)$ and transport coupling strength λ_{tr} of PdCoO₂ and Pd in Fig. S11, with very similar results ($\lambda_{\text{tr}} = 0.056$ for PdCoO₂).

To understand the abnormally small λ of PdCoO₂ we note that λ can be written as²⁶:

$$\lambda = 2N_{\text{F}} \left\langle \left\langle \sum_{\nu} \frac{|g_{m\nu}(\mathbf{k}, \mathbf{k}')|^2}{\hbar\omega_{\mathbf{k}'-\mathbf{k},\nu}} \right\rangle \right\rangle_{\text{FS}}, \quad (2)$$

where $\langle \langle \dots \rangle \rangle_{\text{FS}}$ denotes a double average over the electronic states $m\mathbf{k}$ and $n\mathbf{k}'$ on the Fermi surface. Hence, a key factor that results in the exceptionally small λ of PdCoO₂ is its small DOS N_{F} , which originates from its single, highly dispersive band that crosses the Fermi level.

However, DOS alone cannot fully explain PdCoO₂'s λ value. In particular, if we focus on the acoustic-phonon contribution to λ by setting the upper limit of the frequency integration of $\omega^{-1}\alpha^2 F(\omega)$ to $\omega_{\text{max}} = 30$ meV for PdCoO₂, the calculated λ of PdCoO₂ is only $\lambda_{\text{PdCoO}_2}^{\text{acoustic}} = 0.05$. This leads to $\lambda_{\text{Pd}}/\lambda_{\text{PdCoO}_2}^{\text{acoustic}} \approx 7.2$, which is much larger than the corresponding DOS ratio near the Fermi level ($N_{\text{F}}(\text{Pd})/N_{\text{F}}(\text{PdCoO}_2) \approx 5$). The Fermi surface average of $|g|^2/\omega$, therefore, must also play an important role. To elucidate its contribution, we calculate the zeroth-moment frequency integration of $\alpha^2 F(\omega)$, denoted by $\kappa(\omega) = 2 \int_0^{\omega} d\omega' \alpha^2 F(\omega')$. κ provides information regarding the Fermi surface average of $|g|^2$: $\kappa = 2N_{\text{F}} \langle \langle \sum_{\nu} |g_{\nu}(\mathbf{k}, \mathbf{k}')|^2 / \hbar \rangle \rangle_{\text{FS}}$. For phonon frequency up to ω_{max} , we find that $\kappa_{\text{Pd}}/\kappa_{\text{PdCoO}_2}^{\text{acoustic}} \approx 4.9$, which is close to the DOS ratio. Thus, the Fermi surface average of the $|g|^2$, summing over the acoustic phonon branches, are similar between PdCoO₂ and Pd. What contributes to the much smaller λ value of PdCoO₂, in addition to its small DOS, is that the electron-phonon scattering in PdCoO₂ disproportionately occurs in the higher-

frequency acoustic phonon region, as can be seen from the $\alpha^2 F(\omega)$ data in Fig. 3a. This behavior can be understood given that PdCoO₂ has a large, open, and highly faceted Fermi surface, which gives rise to Fermi surface nesting between the parallel sheets of the nearly hexagonal surface. This is quantified in Fig. 3b, where we plot the nesting factor $\xi_{\mathbf{k}'-\mathbf{k}} = \sum_{nm} \int_{\text{BZ}} \frac{d\mathbf{k}}{\Omega_{\text{BZ}}} \delta(\varepsilon_{n\mathbf{k}} - \varepsilon_{\text{F}}) \delta(\varepsilon_{m\mathbf{k}'} - \varepsilon_{\text{F}})$ for different $\mathbf{k}' - \mathbf{k}$ values. The frequency of the phonons that corresponds to the nesting vector is around 20 meV (Fig. S12), in consistent with the main peak of $\alpha^2 F(\omega)$ of PdCoO₂ in Fig. 3a.

Another perspective to understand the contribution of $|g|^2/\omega$ to λ is that the matrix elements $|g|$ corresponding to the Umklapp backscattering are suppressed in PdCoO₂. This is indeed supported by our *ab initio* calculations of the electron-phonon matrix elements $\sum_{\nu} |g_{\nu}(\mathbf{k}, \mathbf{k}')|$ for the acoustic phonon branches in Fig. 3c. When $\mathbf{K} = \mathbf{k}' - \mathbf{k}$ enters into the Umklapp scattering regime, which roughly corresponds to $\theta = \pi/2$ in Fig. 3c, $\sum_{\nu} |g_{\nu}(\mathbf{k}, \mathbf{k}')|$ becomes lower in magnitude (see also Fig. S13). Meanwhile, the phonon frequency ω does not exhibit a significant variation (see Fig. S12). We verify that the change in $|g|$ is not directly correlated with the variation in the overlap of the lattice periodic parts of the wavefunctions $\langle u_{\mathbf{k}'} | u_{\mathbf{k}} \rangle$ (due to Fermi surface orbital-momentum locking²⁴, see Fig. S14). Instead, the result is more consistent with the screening model of electron-phonon interaction¹⁹, in which the electronic screening of the phonon-induced change in nucleus potential plays a pivotal role in determining the strength of electron-phonon coupling. In the simplest version of the model, the electron-phonon matrix elements can be written as¹⁹:

$$g_{\nu}(\mathbf{k}, \mathbf{k}') = -i \sqrt{\frac{\hbar}{2M\omega_{\mathbf{K},\nu}}} \mathbf{K} \cdot \mathbf{e}_{\nu}(\mathbf{K}) \frac{V(\mathbf{K})}{\epsilon(\mathbf{K})}, \quad (3)$$

where $\mathbf{e}_{\nu}(\mathbf{K})$ denotes the polarization vector of the

phonon mode $\mathbf{K}\nu$, $V(\mathbf{K}) = -4\pi e^2/|\mathbf{K}|^2$ the Fourier transform of the electron-nucleus potential energy, $\epsilon(\mathbf{K})$ the dielectric function, and M the nucleus mass. If neglecting the exchange-correlation contribution, $\epsilon(\mathbf{K})$ can be approximated by the Lindhard dielectric function $\epsilon(\mathbf{K}) = 1 + q_{\text{LH}}^2(\mathbf{K})/|\mathbf{K}|^2$, where $q_{\text{LH}}^2(\mathbf{K}) = -4\pi e^2\chi_0(\mathbf{K})$, with $\chi_0(\mathbf{K})$ being the static bare susceptibility: $\chi_0(\mathbf{K}) = \frac{2}{N_{\mathbf{k}}\Omega} \sum_{\mathbf{k}} \frac{f_{\mathbf{k}+\mathbf{K}} - f_{\mathbf{k}}}{\epsilon_{\mathbf{k}+\mathbf{K}} - \epsilon_{\mathbf{k}}}$. The screened potential energy $V(\mathbf{K})/\epsilon(\mathbf{K})$ in Eq. 3 can then be written as $-4\pi e^2 [\mathbf{K}^2 + q_{\text{LH}}^2(\mathbf{K})]^{-1}$. In Fig. S15 and S16, we have further ruled out the polarization factor $\mathbf{K} \cdot \mathbf{e}_{\nu}(\mathbf{K})$ in Eq. 3 as the source of the matrix-element suppression. Instead, Fig. S17 indicates that, due to the Fermi surface nesting, $-\chi_0(\mathbf{K})$ and $q_{\text{LH}}(\mathbf{K})$ are significantly larger in the backscattering directions, which, in combination with the large $|\mathbf{K}|$ involved, leads to much smaller $[\mathbf{K}^2 + q_{\text{LH}}^2(\mathbf{K})]^{-1}$ and hence weakened $V(\mathbf{K})/\epsilon(\mathbf{K})$. We thus conclude that the electron-phonon backscattering in PdCoO₂, while favoured by the Fermi surface nesting, is simultaneously associated with weak electron-phonon matrix elements, which are most likely caused by the enhanced electronic screening and a large Umklapp momentum transfer.

In summary, our comprehensive study unravels that the extremely high in-plane conductivity of PdCoO₂ originates from the combination of both high Fermi velocity and exceptional weak electron-phonon coupling ($\lambda = 0.057$). The later is a result of the relatively low electronic density of states at the Fermi level, as well as the large, strongly faceted Fermi surface that leads to Fermi surface nesting and suppressed Umklapp electron-phonon matrix elements. Our work provides significant insights into the electron-phonon coupling in delafossite metals and informs the design of unconventional metals with ultralong carrier lifetimes and superior room-temperature conductivities.

We gratefully acknowledge the support by NSFC under Project No. 62004172 and Research Center for Industries of the Future at Westlake University under Award No. WU2022C041. W.L. thanks Prof. Qiyang Lu for drawing his attention to the delafossite metal system and for helpful discussions. W.L. is also indebted to Prof. Andrew Mackenzie for discussions and very helpful comments on the manuscript. The authors thank Jiaming Hu for useful discussions and the Westlake University HPC Center for computational support.

* liwenbin@westlake.edu.cn

- [1] R. D. Shannon, D. B. Rogers, and C. T. Prewitt, Chemistry of noble metal oxides. I. syntheses and properties of ABO₂ delafossite compounds, *Inorg. Chem.* **10**, 713 (1971).
 [2] R. D. Shannon, C. T. Prewitt, and D. B. Rogers, Chem-

- istry of noble metal oxides. II. crystal structures of platinum cobalt dioxide, palladium cobalt dioxide, copper iron dioxide, and silver iron dioxide, *Inorg. Chem.* **10**, 719 (1971).
 [3] R. D. Shannon, D. B. Rogers, C. T. Prewitt, and J. L. Gillson, Chemistry of noble metal oxides. III. electrical transport properties and crystal chemistry of ABO₂ compounds with the delafossite structure, *Inorg. Chem.* **10**, 723 (1971).
 [4] A. P. Mackenzie, The properties of ultrapure delafossite metals, *Rep. Prog. Phys.* **80**, 032501 (2017).
 [5] R. Daou, R. Frésard, V. Eyert, S. Hébert, and A. Maignan, Unconventional aspects of electronic transport in delafossite oxides, *Sci. Technol. Adv. Mater.* **18**, 919 (2017).
 [6] C. W. Hicks, A. S. Gibbs, A. P. Mackenzie, H. Takatsu, Y. Maeno, and E. A. Yelland, Quantum oscillations and high carrier mobility in the delafossite PdCoO₂, *Phys. Rev. Lett.* **109**, 116401 (2012).
 [7] H. Takatsu, J. J. Ishikawa, S. Yonezawa, H. Yoshino, T. Shishidou, T. Oguchi, K. Murata, and Y. Maeno, Extremely large magnetoresistance in the nonmagnetic metal PdCoO₂, *Phys. Rev. Lett.* **111**, 056601 (2013).
 [8] P. J. W. Moll, P. Kushwaha, N. Nandi, B. Schmidt, and A. P. Mackenzie, Evidence for hydrodynamic electron flow in PdCoO₂, *Science* **351**, 1061 (2016).
 [9] N. Kikugawa, P. Goswami, A. Kiswandhi, E. S. Choi, D. Graf, R. E. Baumbach, J. S. Brooks, K. Sugii, Y. Iida, M. Nishio, S. Uji, T. Terashima, P. Rourke, N. E. Hussey, H. Takatsu, S. Yonezawa, Y. Maeno, and L. Balicas, Interplanar coupling-dependent magnetoresistivity in high-purity layered metals, *Nat. Commun.* **7**, 10903 (2016).
 [10] N. Nandi, T. Scaffidi, P. Kushwaha, S. Khim, M. E. Barber, V. Sunko, F. Mazzola, P. D. C. King, H. Rosner, P. J. W. Moll, M. König, J. E. Moore, S. Hartnoll, and A. P. Mackenzie, Unconventional magneto-transport in ultrapure PdCoO₂ and PtCoO₂, *npj Quantum Mater.* **3**, 66 (2018).
 [11] C. Putzke, M. D. Bachmann, P. McGuinness, E. Zhakina, V. Sunko, M. Konczykowski, T. Oka, R. Moessner, A. Stern, M. König, S. Khim, A. P. Mackenzie, and P. J. Moll, h/e oscillations in interlayer transport of delafossites, *Science* **368**, 1234 (2020).
 [12] G. Varnavides, Y. Wang, P. J. W. Moll, P. Anikeeva, and P. Narang, Mesoscopic finite-size effects of unconventional electron transport in PdCoO₂, *Phys. Rev. Mater.* **6**, 045002 (2022).
 [13] M. D. Bachmann, A. L. Sharpe, G. Baker, A. W. Barnard, C. Putzke, T. Scaffidi, N. Nandi, P. H. McGuinness, E. Zhakina, M. Moravec, S. Khim, M. König, D. Goldhaber-Gordon, D. A. Bonn, A. P. Mackenzie, and P. J. W. Moll, Directional ballistic transport in the two-dimensional metal PdCoO₂, *Nat. Phys.* **18**, 819 (2022).
 [14] H.-J. Noh, J. Jeong, J. Jeong, E.-J. Cho, S. B. Kim, K. Kim, B. I. Min, and H.-D. Kim, Anisotropic electric conductivity of delafossite PdCoO₂ studied by angle-resolved photoemission spectroscopy, *Phys. Rev. Lett.* **102**, 256404 (2009).
 [15] V. Sunko, P. McGuinness, C. Chang, E. Zhakina, S. Khim, C. Dreyer, M. Konczykowski, H. Borrmann, P. Moll, M. König, D. Muller, and A. Mackenzie, Controlled introduction of defects to delafossite metals by electron irradiation, *Phys. Rev. X* **10**, 021018 (2020).
 [16] H.-J. Noh, J. Jeong, J. Jeong, H. Sung, K. J. Park, J.-Y. Kim, H.-D. Kim, S. B. Kim, K. Kim, and B. Min, Orbital

- character of the conduction band of delafossite PdCoO₂ studied by polarization-dependent soft X-ray absorption spectroscopy, *Phys. Rev. B* **80**, 073104 (2009).
- [17] M. Tanaka, M. Hasegawa, T. Higuchi, T. Tsukamoto, Y. Tezuka, S. Shin, and H. Takei, Origin of the metallic conductivity in PdCoO₂ with delafossite structure, *Phys. B: Condens. Matter* **245**, 157 (1998).
- [18] S. Ponc e, W. Li, S. Reichardt, and F. Giustino, First-principles calculations of charge carrier mobility and conductivity in bulk semiconductors and two-dimensional materials, *Rep. Progr. Phys.* **83**, 036501 (2020).
- [19] F. Giustino, Electron-phonon interactions from first principles, *Rev. Mod. Phys.* **89**, 015003 (2017).
- [20] R. Seshadri, C. Felser, K. Thieme, and W. Tremel, Metal-metal bonding and metallic behavior in some ABO₂ delafossites, *Chem. Mater.* **10**, 2189 (1998).
- [21] V. Eyert, R. Fr esard, and A. Maignan, On the metallic conductivity of the delafossites PdCoO₂ and PtCoO₂, *Chem. Mater.* **20**, 2370 (2008).
- [22] K. Kim, H. C. Choi, and B. Min, Fermi surface and surface electronic structure of delafossite PdCoO₂, *Phys. Rev. B* **80**, 035116 (2009).
- [23] K. P. Ong, J. Zhang, J. S. Tse, and P. Wu, Origin of anisotropy and metallic behavior in delafossite PdCoO₂, *Phys. Rev. B* **81**, 115120 (2010).
- [24] H. Usui, M. Ochi, S. Kitamura, T. Oka, D. Ogura, H. Rosner, M. W. Haverkort, V. Sunko, P. D. C. King, A. P. Mackenzie, and K. Kuroki, Hidden kagome-lattice picture and origin of high conductivity in delafossite PtCoO₂, *Phys. Rev. Mater.* **3**, 045002 (2019).
- [25] P. B. Allen, New method for solving Boltzmann's equation for electrons in metals, *Phys. Rev. B* **17**, 3725 (1978).
- [26] G. Grimvall, *The Electron-phonon Interaction in Metals* (North-Holland Publishing Company, 1981).
- [27] S. Y. Savrasov and D. Y. Savrasov, Electron-phonon interactions and related physical properties of metals from linear-response theory, *Phys. Rev. B* **54**, 16487 (1996).
- [28] H. Takatsu, S. Yonezawa, S. Mouri, S. Nakatsuji, K. Tanaka, and Y. Maeno, Roles of high-frequency optical phonons in the physical properties of the conductive delafossite PdCoO₂, *J. Phys. Soc. Jpn.* **76**, 104701 (2007).
- [29] C. C. Homes, S. Khim, and A. P. Mackenzie, Perfect separation of intraband and interband excitations in PdCoO₂, *Phys. Rev. B* **99**, 195127 (2019).